Certain Considerations in Aperture Synthesis of Ultrawideband/Short-Pulse Radiation

Ehud Heyman, *Senior Member, IEEE,* and Timor Melamed

***Abstract*—We consider certain characteristics of the radiation from collimated, ultrawideband short-pulse aperture distributions. It is shown that an efficient radiation must account for the multifrequency nature of the field. Two alternative schemes for wideband aperture synthesis of an impulse-like radiation pattern are examined. The first, entitled the "Iso-width aperture," utilizes only temporal shaping of the excitation pulse. In the other, the "Iso-diffracting aperture," we suggest source shaping in space-time so that all the frequency components in the field have the same collimation distance. The "iso-diffracting" scheme yields higher directivity and more efficient pulsed radiation. Explicit examples for the pulsed source distribution and for the pulsed radiation patterns are presented, parametrized, and contrasted.**

I. Introduction

With the trend toward increased system bandwidth there is a growing interest in the radiation, propagation, and diffraction of ultrawideband/short pulse fields [1]. Of particular interest are well-collimated short pulse fields which are referred to as pulsed beams (PB) or space-time wavepackets [2]–[6]. Because they are well localized in space-time, these wavepackets are useful in modeling applications addressing highly focused energy transfer, local (high resolution) interrogation of targets or of the propagation environment, secured communication, etc., that cannot be obtained by narrow bandwidth (quasi monochromatic) pulses.

This paper explores some general characteristics of scalar radiation from a collimated, ultrawideband short-pulse aperture distribution. This problem can be addressed directly in the time domain since the far zone pulsed radiation pattern is a Radon transform of the initial time-dependent field $u_0(\boldsymbol{x}, t)$ (see discussion in Section V). Ignoring for a moment the role of the evanescent spectrum (which should be included for modeling of realistic sources), the problem of source synthesis for a prescribed pulsed radiation pattern is therefore reduced to an inverse Radon transform [7]. However, even within this simplified framework, not any pulsed radiation pattern may be synthesized efficiently. The time-dependence of the radiation pattern (or equivalently, its frequency content) as a function of the radiation direction, adds degrees of freedom that must be addressed in order to obtain efficient wide-band radiation.

Manuscript received June 10, 1993; revised October 25, 1993. This work is supported in part by the U.S. Air Force Office of Scientific Research under Grant F49620-93-1-0093 and in part by the U.S.-Israel Binational Science Foundation, Jerusalem, Israel, under Grant 88-00204.

The authors are with the Department of Electrical Engineering–Physical Electronics, Faculty of Engineering, Tel-Aviv University, Tel-Aviv 69978, Israel.

IEEE Log Number 9400497.

The present paper addresses this problem from the more traditional frequency domain point of view. It will be shown that an efficient radiation must account for the multifrequency nature of the field. To sharpen the question, let us consider the time-harmonic radiation pattern. Utilizing the Cartesian coordinate frame $\boldsymbol{r} = (x_1, x_2, z) = (\boldsymbol{x}, z)$, the far zone field due to a time-harmonic aperture distribution $\hat{u}_0(\boldsymbol{x}, \omega)$ in the $z = 0$ plane is given by the well known expression

$$\hat{u}(\boldsymbol{r}, \omega) \sim -2ik\frac{e^{ikr}}{4\pi r}\cos\theta\hat{\tilde{u}}_0(\boldsymbol{\kappa}, \omega)|_{\boldsymbol{\kappa}=k\hat{\boldsymbol{r}}_\perp} \tag{1}$$

where $r = |\boldsymbol{r}|$, $\hat{\boldsymbol{r}} = \boldsymbol{r}/r$ is a unit vector in the direction of $\boldsymbol{r}$, $\hat{\boldsymbol{r}}_\perp = \boldsymbol{x}/r$ is the transverse coordinate of $\hat{\boldsymbol{r}}$, $\theta = \sin^{-1}(\rho/r)$, $\rho = |\boldsymbol{x}| = \sqrt{x_1^2 + x_2^2}$, ω is the radian frequency, $k = \omega/v$, v is the wave speed and

$$\hat{\tilde{u}}_0(\boldsymbol{\kappa}, \omega) = \int d^2\boldsymbol{x}\exp(-i\boldsymbol{\kappa}\cdot\boldsymbol{x})\hat{u}_0(\boldsymbol{x}, \omega) \tag{2}$$

is the spatial spectrum of $\hat{u}_0(\boldsymbol{x}, \omega)$. Here and henceforth, over-caretted coordinates are unit vectors and over-caretted field terms denote frequency domain constituents with a suppressed time-dependence $\exp(-i\omega t)$. The amplitude term in (1) contains a time-derivative term $(-i\omega)$ which de-emphasizes the low-frequency components in the far zone. This term must be compensated in order to synthesize an impulse-like radiation pattern. Two alternative approaches are considered in Sections II and III below. In the first, entitled the "Iso-width aperture," the compensation utilizes shaping of the temporal excitation pulse only. In the alternative approach, the "Iso-diffracting aperture," we suggest source shaping in space-time. To construct this scheme we first explain the time-derivative in (1) in terms of fundamental radiation mechanism and show that it is due to the frequency dependence of the aperture's Fresnel distance $F(\omega)$. It therefore follows that synthesizing the aperture so that all frequency components will have the same Fresnel distance yields higher directivity and more efficient pulsed radiation. We also present and contrast explicit examples for the pulsed source distribution and for the resulting pulsed radiation patterns.

The "iso-width" aperture models several high-power pulsed radiation systems [8]–[10] (the so called impulse radiating antenna (IRA); e.g., a quasi TEM horn). Realization of the "iso-diffracting" aperture requires an array of pulsed sources whose amplitude distribution, as well as the their initiation times and pulsewidths, should be tuned per the specifications (e.g., the collimation). Possible candidates to realize this distribution are the new optically triggered photoconducting antennas [11]–[13] (see also articles in [1]). Some general

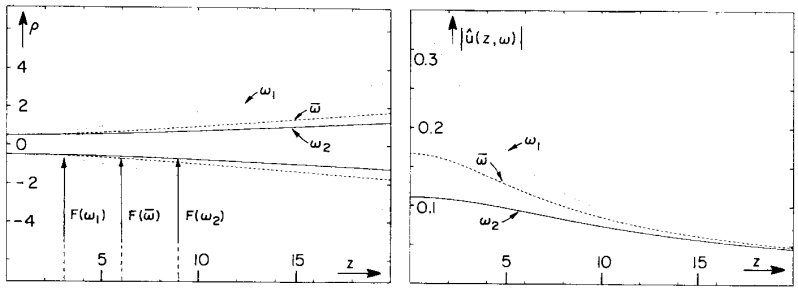

(a) (b)

Fig. 1. Radiation from an ultrawideband iso-width aperture with width W_0. (a) Beamwidth in the (x, z) plane. (b) Field amplitude on the z-axis. The plots are shown at three frequencies: $\omega_1, \omega_2 = 3\omega_1$, and $\bar{\omega}$. Parameters: $W_0 = 1$, $F(\omega_1) = 3W_0$, $F(\omega_2) = 9W_0$.

system parameters of a pulsed driven array have been defined in [3]. The reader should make a clear distinction, however, between possible time-derivatives that characterize small radiating elements (see, e.g., [3]) and between the time-derivative considered in (1). As will be discussed in Section II, the latter is a *global* property of the aperture and is related to the frequency dependence of the Fresnel distance.

II. Iso-Width Aperture

A. General Considerations

It is assumed that $\hat{u}_0(\boldsymbol{x}, \omega)$ can be separated essentially in the form

$$\hat{u}_0(\boldsymbol{x}, \omega) = \hat{f}(\omega)A(\boldsymbol{x}) \tag{3}$$

where the spatial distribution $A(\boldsymbol{x})$ is frequency independent. To generate an impulse-like radiation pattern, the excitation signal $\hat{f}(\omega)$ must compensate the $(-i\omega)$ term in (1), namely [8]–[10]

$$\hat{f} \simeq (-i\omega)^{-1}, \qquad \omega_1 < \omega < \omega_2 \tag{4}$$

where $\omega_{1,2}$ define the usable frequency band. Although this signal emphasizes the low frequencies, it will be explained below that the effective gain of the pulsed aperture (3) is determined by the high-frequency end of the spectrum. Consequently, most of the lower frequency energy in the excitation signal (4) is lost by diffraction.

To understand the difficulties in the realization (3) we now explain the time-derivative in (1) in terms of fundamental wave process. We assume that the spatial distribution $A(\boldsymbol{x})$ is localized about $\boldsymbol{x} = 0$ with an rms width Δ_x, and that it is well collimated, namely that $\Delta_x \gg \lambda = 2\pi/k$ for all ω in the frequency band. The Fresnel length and the diffraction angle are given, respectively, by

$$F(\omega) = k\Delta_x^2, \qquad \Theta(\omega) \simeq (k\Delta_x)^{-1} \tag{5a, b}$$

(Equation (5b) follows from (1) upon using the uncertainty principle $\Delta_\kappa \geq \Delta_x^{-1}$ where Δ_κ is the spectral width.) Under these conditions, one finds that for $z \leq F(\omega)$ the radiated field stays essentially collimated in a beam fashion while for $z \gg F(\omega)$, the field decays like z^{-1} and diverges along the diffraction angle Θ [Fig. 1(a)]. Along the beam axis, the field amplitude may therefore be roughly described by

$$|\hat{u}(z, \omega)| \simeq |\hat{u}_0(\omega)|F(\omega)/\sqrt{F^2(\omega) + z^2} \tag{6a}$$

$$\rightarrow |\hat{u}_0(\omega)|F(\omega)z^{-1} = |\hat{u}_0(\omega)|k\Delta_x^2 z^{-1} \tag{6a}$$

where (6b) is the limit of (6a) for $z \gg F(\omega)$. Equation (6b) clearly shows that the time-derivative term $-ik$ in the far zone amplitude (1) is a direct consequences of the shorter collimation distance $F(\omega)$ and the resulting stronger decay at lower frequencies, as illustrated in Fig. 1(b). This figure also demonstrates how the pulse spectrum in (4) compensates for the shorter collimation distance and for the resulting stronger decay at low frequencies.

The discussion above illustrates the main disadvantage in the iso-width realization of the impulse antenna. The relatively strong energy which must be supplied at low frequencies is lost by large angle diffraction at relatively short distances and does not contribute to the impulse-like wavepacket along the z-axis. The amplitude of the axial pulse is determined essentially by the magnitude of the high-frequency components in the source. Furthermore, for certain applications the strong (parasitic) radiation field at large angles is undesirable and should be avoided. On the other hand, for certain radiating systems, the strong low-frequency fields which are lost by diffraction, are generated relatively easy and at a low cost. Several high power, wide-band radiating systems (e.g., the large quasi TEM horn [10]) are modeled by the iso-width realization.

B. Example: Gaussian Distribution

This close-form example demonstrates the general considerations discussed above. Let

$$\hat{u}_0(\boldsymbol{x}, \omega) = \hat{f}(\omega)e^{-\rho^2/2W_0^2} \tag{7}$$

where the aperture width W_0 is frequency independent. Assuming that $kW_0 \gg 1$, the radiating field in the paraxial region is given by

$$\hat{u}(\boldsymbol{r}, \omega) = \hat{f}(\omega)\frac{-iF(\omega)}{z - iF(\omega)}\exp\left[ik\left(z + \frac{\frac{1}{2}\rho^2}{z - iF(\omega)}\right)\right], \tag{8}$$

with

$$F(\omega) = kW_0^2. \tag{8a}$$

Expression (8) is a Gaussian beam whose cross-sectional width is

$$W(z, \omega) = W_0\sqrt{1 + z^2/F^2(\omega)}. \tag{9}$$

Thus, for $z < F(\omega)$ the beam stays collimated, but for $z \gg F(\omega)$ it diverges along the diffraction angle $\Theta(\omega) = (kW_0)^{-1}$. The amplitude in (8) behaves like $-iF(\omega)/[z - iF(\omega)] \to -iF(\omega)r^{-1} = -ikW_0^2r^{-1}$ where the last term applies for $z \gg F(\omega)$. This behavior is in agreement with (6a, b). In the exponent of (8) we may use for $z \gg F(\omega)$: $z + (1/2)\rho^2/[z - iF(\omega)] \to z + 1/2\rho^2/z + (i/2)\rho^2F(\omega)/z^2 = r + (i/2)F(\omega)\sin\theta$. The result for small θ is

$$\hat{u}(\boldsymbol{r}, \omega) \simeq -ik\hat{f}(\omega)W_0^2\frac{e^{ikr}}{r}e^{-\frac{1}{2}k^2W_0^2\sin^2\theta} \tag{10}$$

which is in agreement with (1) since from (8): $\hat{u}_0(\boldsymbol{\kappa}, \omega) = \hat{f}(\omega)2\pi W_0^2e^{-(1/2)\kappa^2W_0^2}$ where $\kappa = |\boldsymbol{\kappa}|$. However, the derivation of (10) directly from (8) demonstrates, again, that the time-derivative term $(-ik)$ in (1) is a direct consequences of the shorter Fresnel distance and the resulting greater decay at low frequencies.

C. Example: Time-Domain Expressions

As an explicate example we consider an excitation pulse that generates a band-limited impulsive radiation pattern in the main beam direction. We choose

$$\hat{f}(\omega) = \frac{\Omega}{-i\omega}\hat{p}(\omega; \omega_1, \omega_2) \tag{11}$$

where $\hat{p}(\omega; a, b) = 1$ if $a < \omega < b$ and zero otherwise. We use Ω as a normalization constant.

To evaluate the resulting fields it is convenient to utilize the analytic inverse Fourier transform

$$\overset{+}{f}(t) = \frac{1}{\pi}\int_0^\infty d\omega e^{-i\omega t}\hat{f}(\omega). \tag{12a}$$

The function $\overset{+}{f}(t)$ is the analytical signal associated with the frequency spectrum $\hat{f}(\omega)$. From (12a), it is analytic in $\mathrm{Im}\, t \le 0$. The *real* signal $f(t)$ is recovered from the real t limit of $\overset{+}{f}$ via

$$\overset{+}{f}(t) = f(t) + i\mathcal{H}f(t), \qquad t \text{ real} \tag{12b}$$

where $\mathcal{H}$ is the Hilbert transform.

The excitation pulse corresponding to the frequency spectrum (11) is given by

$$f(t) = \int_{-\infty}^t dt'\Omega p(t'; \omega_1, \omega_2) \tag{13}$$

where $p(t; \omega_1, \omega_2)$ is the time-domain counterpart of $\hat{p}(\omega; \omega_1, \omega_2)$,

$$p(t; \omega_1, \omega_2) = \pi^{-1}B\frac{\sin\frac{1}{2}Bt}{\frac{1}{2}Bt}\cos\overline{\omega}t,$$
$$B \equiv \omega_2 - \omega_1, \quad \overline{\omega} \equiv \tfrac{1}{2}(\omega_1 + \omega_2). \tag{14}$$

(Note that $p(t)$ is an even function and that $\int_{-\infty}^\infty p(t')\,dt' = 0$ hence the lower integration limit in (13) can be set to 0.) Plots of $f(t)$ for two values of the fractional bandwidth $\beta = \frac{1}{2}B/\overline{\omega}$, as a function of the normalized time $\overline{t} = \overline{\omega}t$ are depicted in Fig. 2(a). Note that as $\beta \to 1$ the signal tends to $\mathrm{sgn}(t)*\mathrm{sinc}(2\overline{\omega}t)$ where $*$ denotes a convolution. (Also note that the limit $\beta \to 1$, with $\overline{\omega}$ kept constant, implies $\omega_1 \to 0$ and $\omega_2 \to 2\overline{\omega}$. The reader may therefore prefer different normalizations of the results, say keeping ω_1 constant.)

The far zone field has the form

$$u(\boldsymbol{r}, t) \sim r^{-1}g(t - r/v, \theta) \tag{15}$$

where the pulsed radiation pattern is found by applying (12a) to (10) with (11). In view of (12b) it may be expressed conveniently as $g(t, \theta) = \mathrm{Re}\,\overset{+}{g}(t, \theta)$ where the analytic signal $\overset{+}{g}$ is given by

$$\overset{+}{g}(t, \theta) = (\Omega/v)W_0^2(\sqrt{2\pi}\,\overline{\theta})^{-1}e^{-t^2/2\overline{\theta}^2}$$
$$\cdot\{\mathrm{erfc}[(it\overline{\theta}^{-1} + \omega_1\overline{\theta})/\sqrt{2}] - \mathrm{erfc}[(it\overline{\theta}^{-1} + \omega_2\overline{\theta})/\sqrt{2}]\}. \tag{16}$$

In this expression

$$\overline{\theta} = v^{-1}W_0\sin\theta, \tag{17}$$

so that $\omega_j\overline{\theta} = \sin\theta/\Theta(\omega_j)$, $j = 1, 2$, measures the observation direction relative to the diffraction angle $\Theta(\omega_j) = (k_jW_0)^{-1}$ at frequency ω_j [cf. (5)]. Also in (16)

$$\mathrm{erfc}(\sigma) = \frac{2}{\sqrt{\pi}}\int_\sigma^\infty dy\, e^{-y^2} \tag{18}$$

is the complementary error function. To understand the signal in (16) we make use of the large argument approximation

$$\mathrm{erfc}(\sigma) \sim 2H(-\mathrm{Re}\,\sigma) + (\sigma\sqrt{\pi})^{-1}e^{-\sigma^2} \tag{19}$$

where the Heaviside function H equals to 0 or 1 for positive or negative argument, respectively. Noting that the arguments of the erfc functions in (16) have positive real parts it follows that for $\omega_1\overline{\theta} > 1$,

$$\overset{+}{g}(t, \theta) = (\Omega/v)W_0^2\pi^{-1}$$
$$\cdot\left[\frac{e^{-i\omega_1 t - \omega_1^2\overline{\theta}^2/2}}{it + \omega_1\overline{\theta}^2} - \frac{e^{-i\omega_2 t - \omega_2^2\overline{\theta}^2/2}}{it + \omega_2\overline{\theta}^2}\right]. \tag{20}$$

The terms inside the brackets are Lorenzian pulses $(\pi i)^{-1}(t - i\omega_j\overline{\theta}^2)$, $j = 1, 2$, modulated by $\exp(-i\omega_j t)$. Since $\omega_j\overline{\theta} > 1$, the 3 dB pulse length of the Lorenzian, $2\omega_j\overline{\theta}^2$ is longer than the oscillation period $(\omega_j)^{-1}$. Furthermore, the conditions $\omega_1\overline{\theta} = \sin\theta/\Theta(\omega_1) > 1$ implies that θ is outside the main beam direction at the lower frequency ω_1. Consequently the amplitude $\exp(-\omega_1^2\overline{\theta}^2/2)$ of first term in (20) is exponentially weak while, since $\omega_2 \gg \omega_1$, the second term may be neglected altogether. Expression (20) is also valid if $\omega_1\overline{\theta} < 1$, provided that $t\overline{\theta}^{-1} \gg 1$. In the limit $\theta \to 0$, $\overset{+}{g}$ reduces therefore to

$$\overset{+}{g}(t, \theta)|_{\theta=0} = (\Omega/v)W_0^2(\pi it)^{-1}(e^{-i\omega_1 t} - e^{i\omega_2 t})$$
$$= (\Omega/v)W_0^2\overset{+}{p}(t; \omega_1, \omega_2) \tag{21}$$

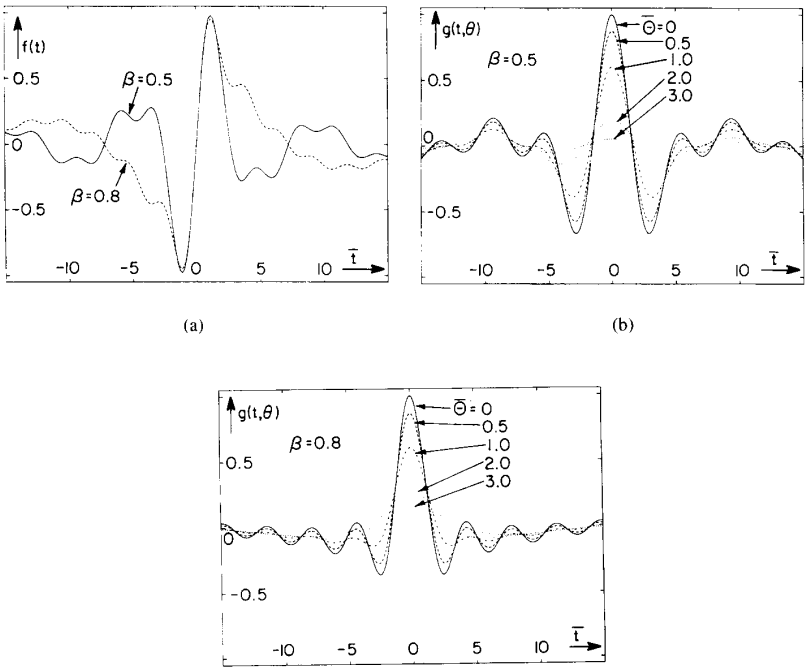

Fig. 2. Short pulsed radiation from an iso-diffracting aperture. (a) The normalized pulsed aperture distribution (30) $\mathrm{Re}\,\overset{+}{u}_0(\boldsymbol{x}, t)[\pi/B]$ for the pulse $\overset{+}{f} = i\overset{+}{p}$ in (39) and for fractional bandwidth $\beta = 0.5$. The excitation is shown as a function of the normalized time $\bar{t} = \bar{\omega}t$ and for several values of the normalized transverse coordinate $\bar{\rho} = \rho/W_0(\bar{\omega})$. (b) The normalized far zone pulse (37) $\mathrm{Re}\,\overset{+}{g}(t, \bar{\theta}[\pi/BF]$ due to the excitation in (a). The observation angle is quantified by the normalized coordinate $\bar{\Theta} = \sin\theta/\Theta(\bar{\omega})$. (c) and (d) As in (a) and (b), respectively, but for $\beta = 0.8$.

where the analytic signal $\overset{+}{p}(t)$ is given by [cf. (14)]

$$\overset{+}{p}(t; \omega_1, \omega_2) = \pi^{-1}B\frac{\sin\frac{1}{2}Bt}{\frac{1}{2}Bt}e^{-i\bar{\omega}t}. \tag{22}$$

The far zone pulse (16) due to the two excitation pulses in Fig. 2(a) are shown in Fig. 2(b) and (c), respectively. The figures show the normalized pulse $g(t, \theta)[\pi v/W_0^2\Omega B]$ as a function of the normalized time $\bar{t} = \bar{\omega}t$. The observation angle θ is quantified by the normalized coordinate $\bar{\Theta} = \sin\theta/\Theta(\bar{\omega})$ where $\Theta(\bar{\omega})$ is the diffraction angle (5) at the center frequency $\bar{\omega}$. One observes that as a function of the normalized time $\bar{t}$, the field in the large β case is more localized with less oscillations than for the smaller β. Concerning the spatial directivity, the large β field has slightly greater transverse decay and a higher collimation within the main beam zone $\bar{\Theta} < 1$. For large $\bar{\Theta}$, on the other hand, the radiated pulse is stronger in the large β case and the directivity is inferior. This readily follows from the fact that increasing β while keeping $\bar{\omega}$ constant adds more low frequencies with shorter collimation distance $F(\omega)$ and larger diffraction angle $\Theta(\omega)$ (see Fig. 1). In fact, as discussed after (20), the pulsed field in this zone is dominated by the first term in (20) and its peak at $t = 0$ is given by $\mathrm{Re}\,\overset{+}{g}(0, \theta) = (\Omega/v)W_0^2\pi^{-1}\exp(-(1/2)\omega_1^2\bar{\theta}^2)/\omega_1\bar{\theta}^2$. For a given θ, this pulse increases as ω_1 decreases. Finally, the results in Fig. 2 will be contrasted latter on with those for the iso-diffracting aperture in Fig. 4.

III. Iso-Diffracting Aperture

A. General Considerations

To overcome the difficulties discussed in the previous section it is suggested to synthesize the wide-band aperture distribution in the form [cf. (3)]

$$\hat{u}_0(\boldsymbol{x}, \omega) = \hat{f}(\omega)A\left(\sqrt{\frac{\omega}{\omega_0}}\boldsymbol{x}\right) \tag{23}$$

where ω_0 is some reference frequency. To simplify the interpretation of the final results it is convenient to choose $\omega_0 \equiv \omega_2$ where ω_2 denotes the upper limit of the frequency band. It than follows that the aperture width $\Delta_x(\omega)$ is narrowest at ω_2 and for $\omega < \omega_2$ it is given by (see Fig. 3)

$$\Delta_x(\omega) = \sqrt{\frac{\omega_2}{\omega}}\Delta_x(\omega_2). \tag{24}$$

From (5), the Fresnel distance is frequency independent

$$F(\omega) = F(\omega_2) = k_2\Delta_x^2(\omega_2) \tag{25}$$

hence the far zone field does not contain the time-derivative term $(-i\omega)$. Indeed, by applying (2) to (23) one finds that

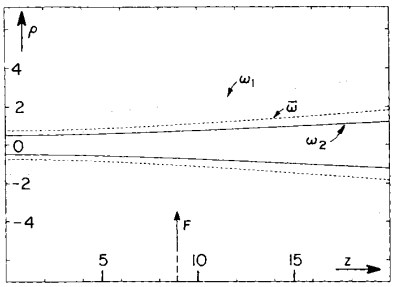

Fig. 3. Radiation from an ultrawideband iso-diffracting aperture with a Fresnel distance F. The figure depicts the beamwidth in the (x, z) plane at three frequencies: ω_1, $\omega_2 = 3\omega_1$, and $\bar{\omega}$. Parameters: $F = 9$, $W_0(\omega_2) = F/9$, $W_0(\omega_1) = \sqrt{3}W_0(\omega_2)$.

$\hat{u}_0(\boldsymbol{\kappa}, \omega) = \hat{f}(\omega)(\omega_2/\omega)\overline{A}(\sqrt{\omega_2/\omega}\boldsymbol{\kappa})$, where $\overline{A}(\boldsymbol{\kappa})$ is the spatial spectrum of $A(\boldsymbol{x})$, so that (1) yields

$$\hat{u}(\boldsymbol{r}, \omega) \sim -2ik_2 \frac{e^{ikr}}{4\pi r}\cos\theta \hat{f}(\omega)\overline{A}(\boldsymbol{\kappa})\Big|_{\boldsymbol{\kappa}=\sqrt{k_2}k\hat{\boldsymbol{r}}_\perp}. \quad (26)$$

It now follows that for $\omega < \omega_2$ the far zone pattern (1) is weaker by the ratio (ω/ω_2) relative to the pattern in (26). This is, of course, a consequence of the wider aperture needed by the iso-diffracting realization for $\omega < \omega_2$ (see (24) and Fig. 3). Finally, a different way to look at the iso-diffracting distribution (23) is to consider the frequency content of the source-elements in the aperture: At the center, for $\rho < \Delta_x(\omega_2)$, the high-frequency bound of these elements is $\omega_{\max} = \omega_2$, but for $\rho > \Delta_x(\omega_2)$ the frequency bound is $\omega_{\max}(\rho) = \omega_2\sqrt{\Delta_x(\omega_2)/\rho} < \omega_2$.

B. Example: Gaussian Distribution

The Gaussian distribution that satisfy condition (23) has the form

$$\hat{u}_0(\boldsymbol{x}, \omega) = \hat{f}(\omega)e^{-k\rho^2/2F} \quad (27)$$

where F is now a frequency independent constant. The width of this distribution depends on the frequency via [cf. (8a)]

$$W_0(\omega) = \sqrt{F/k}. \quad (28)$$

The time-harmonic radiating field is given by (8) but with F being a constant, namely

$$\hat{u}(\boldsymbol{r}, \omega) = \hat{f}(\omega)\frac{-iF}{z-iF}\exp\left[ik\left(z + \frac{\frac{1}{2}\rho^2}{z-iF}\right)\right]. \quad (29)$$

For $z \gg F$ the amplitude of this term yields $-iF/(z-iF) \to -iFz^{-1}$ hence, since F is frequency independent, the far zone field is *not* a time-derivative of the aperture signal. Indeed, following the procedure outlined in (10), the far zone field is given by

$$\hat{u}(\boldsymbol{r}, \omega) \simeq -i\hat{f}(\omega)\frac{e^{ikr}}{r}Fe^{-\frac{1}{2}kF\sin^2\theta}. \quad (30)$$

C. Time-Domain Expressions

The field solutions in (27)–(30) may readily be transformed to the time domain. Utilizing the analytic inverse Fourier transform (12a) one finds that the analytical initial pulsed field is given by

$$\overset{+}{u}_0(\boldsymbol{x}, t) = \overset{+}{f}\left(t - \frac{i}{2}\rho^2/vF\right) \quad (31)$$

where $\overset{+}{f}(t)$ is the analytic signal associated with the frequency spectrum $\hat{f}(\omega)$. The *real* pulsed distribution that give rise to the real radiating field is found by taking the real part of (31). The properties of this distribution are due to the fact that analytic signals generally decay as the imaginary part of their argument becomes more negative. Noting that the imaginary part of the argument of $\overset{+}{f}$ in (31) becomes negative as ρ increases, it follows that the excitation pulse is strongest at the center of the aperture and decays away from the center. Specific example will be considered later on.

The analytic pulsed field due to the aperture distribution (31) is obtained by applying (12a) to (29), giving

$$\overset{+}{u}(\boldsymbol{r}, t) = \frac{-iF}{z-iF}\overset{+}{f}[t - z/v - \tfrac{1}{2}\rho^2/v(z-iF)]. \quad (32)$$

This expression describes a wavepacket that propagates along the z-axis. It is identical with the paraxial approximation of the so-called complex source pulsed beam (CSPB), which is a globally exact wavepacket solution of the time-dependent wave equation. The global and the paraxial properties of the CSPB have been investigated thoroughly in the past (see, e.g., [5], [6], [14], [15]). Some of the most relevant properties will be discussed below.

As discussed earlier, the transverse confinement in (32) is due to the negative imaginary part the term $-(1/2)p^2/v(z-iF)$ in the argument of $\overset{+}{f}$ in (32). To quantify this behavior we write $(z-iF)^{-1} = R^{-1} + iI^{-1}$, i.e.,

$$R(z) = z + F^2/z, \quad I(z) = F(1 + z^2/F^2) \quad (33)$$

Equation (32) now has the form

$$\overset{+}{u}(\boldsymbol{r}, t) = \frac{-iF}{z-iF}\overset{+}{f}[t - \tau(z, \boldsymbol{x}) - i\gamma(z, \boldsymbol{x})] \quad (34)$$

where

$$\tau(\boldsymbol{r}) = z/v + \tfrac{1}{2}\rho^2/vR(z), \qquad \gamma(\boldsymbol{r}) = \tfrac{1}{2}\rho^2/vI(z). \quad (35a, b)$$

Clearly τ defines the paraxial propagation delay hence R is the wavepacket radius of curvature. The transverse envelope decay of $\overset{+}{u}$ is controlled by $\gamma(\boldsymbol{r})$ since the waveform amplitude decays as γ increases away from the z-axis. The amplitude contour lines (lines of constant γ) are described by the condition $\rho^2/I(z) =$ constant. Thus the wavepacket has a waist at the $z = 0$ plane where I is smallest. Near the waist, for $z \ll F$, $I \simeq F$ and the wavepacket stays collimated, but for $z \gg F$, $I \simeq z^2/F$ hence the amplitude contour lines satisfy $\rho/z =$ const. and the wavepacket opens up along a constant diffraction angle. The discussion above identifies F as the collimation length of the wavepacket. It should be recalled

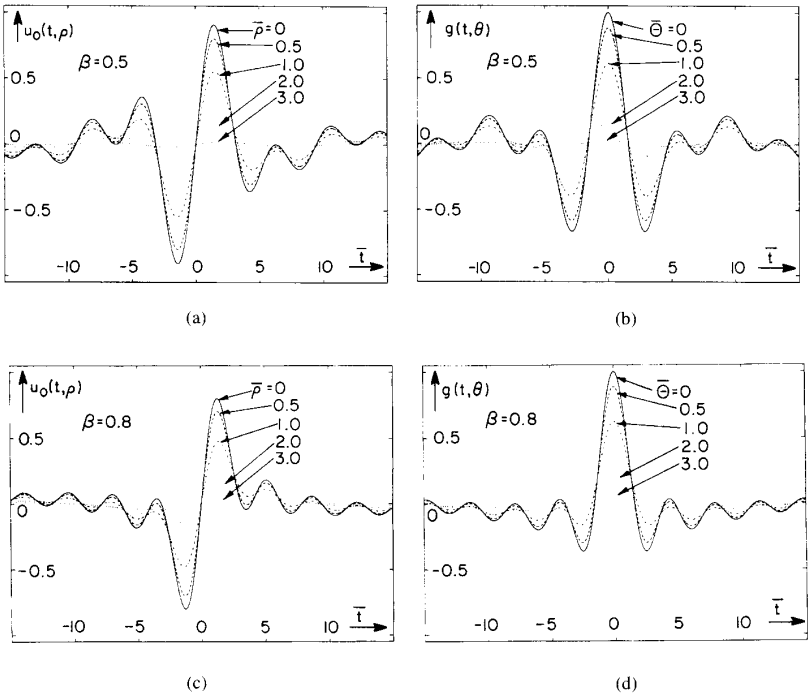

Fig. 4. Short pulsed radiation from an iso-width aperture. (a) The normalized excitation pulse (13) $f(t)[\varpi\pi/B]$ for fractional bandwidth $\beta = (1/2)B/\varpi = 0.5$ and 0.8. (b) and (c) The normalized far zone pulse (16) $g(t, \theta)[\pi v/W_0^2 B]$ for $\beta = 0.5$ and 0.8, respectively. All plots are shown as function of the normalized time $\bar{t} = \varpi t$. The observation directions are quantified by the normalized coordinate $\bar{\Theta} = \sin\theta/\Theta(\varpi)$.

that a key feature in this wavepacket solution is that all its frequency components have the same collimation distance F [see (27)].

To understand the structure of the *real* field we introduce the real waveform $f_\gamma(t)$ via [see (12b)]

$$\overset{+}{f}(t - i\gamma) \equiv f_\gamma(t) + i\mathcal{H}f_\gamma(t). \tag{36}$$

From (34), the real field solution is given now by

$$u(\boldsymbol{r}, t) = [1 + (z/F)^2]^{-1}\left\{1 + \frac{z}{F}\mathcal{H}\right\}f_\gamma(t - \bar{\tau}). \tag{37}$$

Since the real waveforms f_γ decay as γ grows, $u(\boldsymbol{r}, t)$ is strongest on the z axis (where $\gamma = 0$ and $f_\gamma \equiv f$) and decays as γ increases away from the axis. One also observes that the waveforms in (37) are gradually Hilbert transformed along the propagation paths. For the special case on the z-axis, $f_\gamma(t) \equiv f(t)$ and the waveform changes from $f(t - z/v)$ for $z \ll F$ to $z^{-1}F\mathcal{H}f(t - z/v)$ as $z \to \infty$ (i.e., a Hilbert transform of the near zone signal). Finally, from (32), using $z + (1/2)\rho^2/(z - iF) \to r + (i/2)F\sin\theta$ [see (10)], the far zone pulsed field has the form (15) with the analytic radiation pattern

$$\overset{+}{g}(t, \theta) = -iF\overset{+}{f}\left(t - \frac{i}{2}v^{-1}F\sin^2\theta\right). \tag{38}$$

The real radiation is obtained by taking the real part of (38).

D. Example for a Specific Pulse

As a specific example for an excitation pulse we consider a pulse that generates the same pulsed radiation pattern in the main beam direction as in the example of Section II-B. This pulse has the frequency spectrum

$$\hat{f}(\omega) = i\hat{p}(\omega; \omega_1, \omega_2) \tag{39}$$

with $\hat{p}$ defined in (11), hence

$$\overset{+}{f}(t) = i\overset{+}{p}(t; \omega_1, \omega_2) \tag{40}$$

where $\overset{+}{p}$ is defined in (22) [see also (14)]. From (32) and (38) the pulsed aperture distribution and the corresponding far zone pulsed radiation pattern are given now by $u_0(\boldsymbol{x}, t) = \mathrm{Re}\, i\overset{+}{p}(t - (i/2)\rho^2/vF; \omega_1, \omega_2)$ and $g(t, \theta) = F\,\mathrm{Re}\,\overset{+}{p}(t - (i/2)v^{-1}F\sin^2\theta; \omega_1, \omega_2)$. Note that we intentionally introduced an i in (39) so that $g(t, \theta)|_{\theta=0} = Fp(t)$ has the same waveform as in the example of Section II (see (21) and Fig. 2). With this choice, $u_0|_{\rho=0} = -\mathrm{Im}\,\overset{+}{p}(t) = -\mathcal{H}p(t)$ and is given by (14) with cos $\to$ −sin (see Fig. 4).

Fig. 4 shows the normalized pulsed aperture distribution $u_0(\boldsymbol{x}, t)[\pi/B]$ and the corresponding normalized far zone pulsed radiation pattern $g(t, \theta)[\pi/FB]$. Parts (a) and (b) depict the aperture distribution and the radiated pulse for fractional bandwidth $\beta = 0.5$, while Parts (c) and (d) correspond to $\beta = 0.8$. All plots are shown as a function of the normalized time $\bar{t} = \varpi t$. The radial coordinate ρ in the aperture is quantified by

the normalized coordinate $\overline{\rho} = \rho/\sqrt{\overline{\omega}/vF} = \rho/W_0(\overline{\omega})$ with $W_0(\overline{\omega})$ being the aperture width (28) at the center frequency $\overline{\omega}$. The observation directions are quantified by the normalized coordinate $\overline{\Theta} = \sqrt{kF}\sin\theta = \sin\theta/\Theta(\overline{\omega})$ with $\Theta(\overline{\omega})$ being the diffraction angle at $\overline{\omega}$. From the results one may readily confirm the Hilbert transform relation between the aperture field in (a) and (c) and the far zone fields in (b) and (d), respectively. Note that as mentioned earlier, the axial radiation pattern g is proportional to $p(t)$, while the axial excitation u_0 is proportional to $-\mathcal{H}p(t)$. Comparing the waveforms in Fig. 4 to those in Fig. 2, one finds that the iso-diffracting aperture has better directivity than the iso-width aperture. This has been explained by the fact that the iso-width aperture radiate strong low frequency components at relatively large diffraction angles (cf. Figs. 1 and 3).

IV. Aperture Efficiency

In this section we show that due to the larger low-frequency diffraction losses, the iso-width aperture distribution is less efficient than the iso-diffracting distribution. We shall compare the gain G, defined in an energy sense by

$$G = \frac{2\pi r^2 S_0}{E_0} \tag{41}$$

where

$$E_0 = \int d^2\boldsymbol{x}\|u_0(\boldsymbol{x}, t)\|^2, \qquad S_0 = \|u(\boldsymbol{r}, t)\|^2_{\substack{r\to\infty \\ \theta=0}} \tag{42}$$

being, respectively, the total source energy and the energy flow density of the axial radiation field, with $\|f(t)\|^2 = \int_{-\infty}^{\infty}|f(t)|^2\,dt$. Utilizing Parseval's theorem, one readily finds from (7) and (10) with (11) that in the iso-width case $E_0 = \Omega^2 W_0^2(\omega_1^{-1} - \omega_2^{-1})S_0 = (\Omega/v)^2 W_0^4 B/\pi r^2$, hence

$$G_{\text{iso-width}} = 2v^{-2}W_0^2\omega_1\omega_2. \tag{43}$$

Similarly, from (27) and (30) with (39) one finds for the iso-diffracting case $E_0 = vF\ln(\omega_2/\omega_1)S_0 = F^2B/\pi r^2$, hence

$$G_{\text{iso-diff}} = 2FB/v\ln(\omega_2/\omega_1). \tag{44}$$

To compare the two models we shall calculate the ratio

$$\mathcal{G} \equiv \frac{G_{\text{iso-diff}}}{G_{\text{iso-width}}}. \tag{45}$$

In order to compare the two models we also have to normalize them by assuming that they have the same aperture width at some reference frequency ω_0. We shall consider three alternative normalizations wherein ω_0 is either ω_1, $\overline{\omega}$, or ω_2 (note, that the first normalization implies that the iso-diffracting aperture is narrower than the iso-width aperture for all $\omega > \omega_1$, while the third implies that it is wider for all $\omega < \omega_2$). Under these conditions, W_0 in (43) and F in (44) are related by [see (28)] $F = v^{-1}\omega_0 W_0^2$ where $\omega_0 = \omega_1$, $\overline{\omega}$, or ω_2, respectively. Denoting the corresponding values of $\mathcal{G}$ as $\mathcal{G}_1$, $\overline{\mathcal{G}}$, and $\mathcal{G}_2$, respectively, we obtain

$$\mathcal{G}_1 = \frac{2\beta}{(1+\beta)\ln\frac{1+\beta}{1-\beta}}, \quad \overline{\mathcal{G}} = \mathcal{G}_1\frac{1}{1-\beta}, \quad \mathcal{G}_2 = \mathcal{G}_1\frac{1+\beta}{1-\beta}. \tag{46}$$

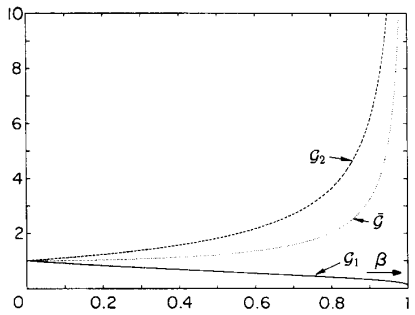

Fig. 5. The ratio $\mathcal{G}$ of the pulsed aperture gains as a function of the fractional bandwidth β [see (46)].

A plot of the relative gains $\mathcal{G}$ as a function of the fractional bandwidth β are shown in Fig. 5. Note that $\mathcal{G} \to 1$ for $\beta \to 0$ (monochromatic case).

One may also be interested in comparing the axial energy flux S_0 of the two models. Defining

$$\mathcal{S} \equiv \frac{S_{0_{\text{iso-diff}}}}{S_{0_{\text{iso-width}}}} \tag{47}$$

we find that $\mathcal{S} = (vF/\Omega W_0^2)^2$. Again, to compare the two models we assume that they have the same aperture width at some reference frequency ω_0. Consequently, $F = v^{-1}\omega_0 W_0^2$ and

$$\mathcal{S} = \frac{\omega_0^2}{\Omega^2}. \tag{48}$$

Comparing (11) with (39), this implies that in order to obtain the same pulse energy in the main beam direction, the spectral amplitude of the iso-width aperture distribution and the spectral amplitude of the iso-diffracting field at the center of the aperture must have the same magnitude at ω_0. Note from (27), however, that the spectral amplitude in the iso-diffracting aperture decays away from the center.

V. Concluding Remarks

It has been demonstrated that efficient well collimated pulsed radiation patterns can be synthesized by space-time shaping of the aperture distribution. The effect of the frequency dependence of the Fresnel distance has been established by exploring in details two realizations: the "iso-width" and the "iso-diffracting" distributions (for a different class of realizations, see [16]). It has been demonstrated that the axial-wavepacket excitation is more efficient in the latter. In this paper we utilized the more traditional frequency domain analysis but, because of the short pulsed structure of the field, it is important to explore the radiation process directly in the time domain. Here the governing spectral framework is the Radon transform. Specifically, the far zone time-dependent field has the form (15) wherein the radiation pattern $g(t, \hat{\boldsymbol{r}})$ can be expressed in the form

$$g(t, \hat{\boldsymbol{r}}) = -(2\pi v)^{-1}\cos\theta\,\partial_t\tilde{u}_0(\boldsymbol{\xi}, t)|_{\boldsymbol{\xi}=\hat{\boldsymbol{r}}_\perp} \tag{49}$$

where

$$\tilde{u}_0(\boldsymbol{\xi}, t) = \int d^2\boldsymbol{x} u_0(\boldsymbol{x}, t + v^{-1}\boldsymbol{\xi} \cdot \boldsymbol{x}). \tag{50}$$

Here $\tilde{u}_0(\boldsymbol{\xi}, t)$ is the Radon transform of the pulsed source distribution $u_0(\boldsymbol{x}, t)$. It describes the transient plane waves that propagates in the $\boldsymbol{\xi}$ direction. Equations (49)–(50) are readily recognized as Fourier transform of the time-harmonic radiation pattern (1)–(2), but they can also be derived directly from the time-dependent spectral integral representations as formulized by the Spectral Theory of Transients (STT) [17].

REFERENCES

[1] H. L. Bertoni, L. Carin, and L. B. Felsen, Eds., *Proceedings of the International Conference on Ultra-Wideband Short Pulse Electromagnetics.* New York: Plenum, 1993.

[2] R. W. Ziolkowski, I. M. Besieris, and A. M. Shaarawi, "Localized wave representations of acoustic and electromagnetic radiation," *Proc. IEEE*, 1991.

[3] R. W. Ziolkowski, "Properties of electromagnetic beams generated by ultra-wide bandwidth pulse-driven arrays," *IEEE Trans. Antennas Propagat.*, vol. AP-40, pp. 888–905, 1992.

[4] H. E. Moses and R. T. Prosser, "Acoustic and electromagnetic bullets. New exact solutions of the acoustic and Maxwell's equation," *SIAM J. Appl. Math.*, vol. 50, pp. 1325–1340, 1990.

[5] E. Heyman and B. Z. Steinberg, "A spectral analysis of complex source pulsed beams," *J. Opt. Soc. Amer., A*, vol. 4, pp. 473–480, 1987.

[6] E. Heyman and L. B. Felsen, "Complex source pulsed beam fields," *J. Opt. Soc. Amer. A*, vol. 6, pp. 806–817, 1989.

[7] H. E. Moses and R. T. Prosser, "Initial conditions, sources, and currents for prescribed time-dependent acoustic and electromagnetic fields in three dimensions. Part I: The inverse initial value problem. Acoustic and Electromagnetic 'bullets,' expanding waves, and imploding waves," *IEEE Trans. Antennas Propagat.*, vol. AP-34, pp. 188–196, 1986.

[8] C. E. Baum, "Radiation of impulse-like transient fields," *Sensor Simulation Notes*, 321, 1989.

[9] ——, "Aperture efficiency for impulse radiating antennas," *Sensor Simulation Notes*, vol. 328, 1991.

[10] R. S. Clark, L. F. Rinehart, M. T. Buttram, and J. F. Aurand, "An overview of Sandia National Laboratories; plams switched gigawatt ultra-wideband impulse transmitter program," in *Ultra-Wideband/Short Pulse Electromagnetics*, H. L. Bertoni, L. Carin, and L. B. Felsen, Eds. New York: Plenum, 1993, pp.93–98.

[11] D. H. Auston, K. P. Cheung, and P. R. Smith, "Picosecond photoconducting Hertzian dipoles," *Appl. Phys. Lett.*, vol. 45, pp. 284–286, 1984.

[12] A. P. DeFonzo and C. R. Luntz, "Optoelectronic transmission and reception of ultrashort electrical pulses," *Appl. Phys. Lett.*, vol. 51, pp. 212–214, 1987.

[13] W. W. Roberstson, G. Arjavalingam, and G. V. Kopcsay, "Picosecond time-domain electromagnetic scattering from conducting cylinders," *IEEE Microwaves Guided Waves Lett.*, vol. 1, pp. 379–381, 1991.

[14] E. Heyman, "Complex source pulsed beams: Properties and applications," *Radio Sci.*, vol. 26, pp. 237–248, 1991.

[15] ——, "Pulsed beam propagation in inhomogeneous medium," *IEEE Trans. Antennas Propagat.*, vol. 42, no. 3, pp. 311–319, March 1994.

[16] R. Donnelly and R. W. Ziolkowski, "Designing localized waves," *Proc. Roy. Soc. Lond., A*, vol. 440, pp. 541–565, 1993.

[17] E. Heyman and L. B. Felsen, "Weakly dispersive spectral theory of transients (STT), Part I: Formulation and interpretation," *IEEE Trans. Antennas Propagat.*, vol. AP-35, pp. 80–86, 1987.

Ehud Heyman (S'80–M'82–SM'88) was born in Tel-Aviv, Israel, on August 29, 1952. After serving in the Israeli army from 1970 to 1974, he received the B.S. degree in electrical engineering, valedictorian summa cum laude, from Tel-Aviv University, Israel, in 1977, the M.S. degree in electrical engineering, with distinction, from the Technion–Israel Institute of Technology, in 1979, and the Ph.D. degree in electrophysics from the Polytechnic Institute of New York (now Polytechnic University), Brooklyn, in 1982.

He held teaching assistant positions during his undergraduate and graduate studies. While at the Polytechnic Institute, he was a Research and latter on a Postdoctoral fellow, as well as a Rothschild, a Fulbright, and a Hebrew Technical Institute fellow. In 1983 he joined the department of physical electronics at the faculty of engineering at Tel-Aviv University where he now holds the position of an Associate Professor. During 1991 and 1992 he spent a sabbatical leave of absence with Northeastern University, Boston, MA, with the Massachusetts Institute of Technology, Cambridge, and with A. J. Devaney Association, Boston. His research interest is in analytic methods in wave theory, including: high-frequency techniques and time-domain techniques for propagation and scattering, directed energy, inverse scattering, target identification, and propagation in random medium.

Dr. Heyman is a member of Sigma Xi, a senior member of IEEE AP-S, and a Chairman of commission B of the Israeli National Committee for Radio Sciences (URSI).

Timor Melamed was born in Tel-Aviv, Israel, in January 1964. He received the B.Sc. degree cum laude in electrical engineering from Tel-Aviv University, Tel-Aviv, Israel in 1989.

He worked at National Semiconductor, Israel, in the design and debug of microprocessors. He is currently studying toward a Ph.D. degree at Tel-Aviv University. His main fields of interest are analytic techniques in wave theory, transient wave phenomena, and inverse scattering.